Eur. Phys. J. E (2015) **38**: 29
DOI 10.1140/epje/i2015-15029-0

THE EUROPEAN
PHYSICAL JOURNAL E

Regular Article

# Contribution to the benchmark for ternary mixtures: Measurement of diffusion and Soret coefficients in 1,2,3,4-tetrahydronaphthalene, isobutylbenzene, and dodecane onboard the ISS*

Oleg A. Khlybov[1], Ilya I. Ryzhkov[2], and Tatyana P. Lyubimova[1,a]

[1] Institute of Continuous Media Mechanics UB RAS, Koroleva St. 1, 614013 Perm, Russia
[2] Institute of Computational Modelling SB RAS, Akademgorodok, 660036 Krasnoyarsk, Russia

Received 1 August 2014 and Received in final form 27 September 2014

**Abstract.** The paper is devoted to processing the data of DCMIX 1 space experiment. In this experiment, the Optical digital interferometry was used to measure the diffusion and Soret coefficients in the ternary mixture of 1,2,3,4–tetrahydronaphthalene, isobutylbenzene and $n$-dodecane at mass fractions of 0.8/0.1/0.1 and at 25 °C. The raw interferometric images were processed to obtain the temporal and spatial evolution of refractive indices for two laser beams of different wavelengths. The method for extracting the diffusion and thermal diffusion coefficients originally developed for optical beam deflection was extended to optical digital interferometry allowing for the spatial variation of refractive index along the diffusion path. The method was validated and applied to processing the data for Soret and diffusion steps in 5 experimental runs. The obtained results for the Soret coefficients and one of the eigenvalues of diffusion matrix showed acceptable agreement within each step. The second eigenvalue was not determined with sufficient accuracy.

## 1 Introduction

Heat and mass transfer in multicomponent mixtures are rather complicated phenomena due to the presence of several transport mechanisms: convection, heat conduction, diffusion, and thermal diffusion. These phenomena play an important role in many natural and technological processes. In particular, diffusion and thermodiffusion affect the distribution of components in hydrocarbon deposits due to the presence of geothermal gradient [1]. Description and prediction of deposit composition is extremely important for their efficient exploitation and oil extraction.

For describing heat and mass transfer in multicomponent mixtures, it is necessary to know the values of transport coefficients (in particular, diffusion and thermal diffusion coefficients). These properties can be measured experimentally or estimated with the help of theoretical models. Existing models can predict diffusion and thermal diffusion coefficients for some classes of binary mixtures with good accuracy. Contrary to that, the theory of transport processes in multicomponent liquid mixtures is far from completeness. Experimental verification of theoretical models is complicated because of the lack or even absence of experimental data for mixtures with three or higher number of components. The development of measurement methods and accurate data on diffusion and thermodiffusion coefficients are extremely important for advancing the theory of transport phenomena in mixtures and its applications to natural and technological processes.

Modern optical methods provide high accuracy of transport coefficient measurement since they do not disturb the diffusion process [2,3]. The paper [4] is probably one of the first works, where diffusion and Soret coefficients in binary mixtures were measured simultaneously by optical technique (interferometry). A necessary condition for the application of optical methods is the absence of convection. The mixture must remain in the stable mechanical equilibrium state. It means that the temperature gradient should be strictly anti-parallel to the gravitational acceleration vector in terrestrial conditions. However, for mixtures with negative Soret effect, the heavier components move to the warmer areas, which leads to convective instability in gravity field. Convection may arise even in the case of potentially stable stratification if the thermal and diffusion time scales are essentially different [5]. The instabilities of such type can develop in various experimental configurations. On the Earth, convection could appear in theoretically stable configurations

---

[*] Contribution to the Topical Issue “Thermal non-equilibrium phenomena in multi-component fluids” edited by Fabrizio Croccolo and Henri Bataller.

[a] e-mail: `lubimova@psu.ru`

due to the imperfectness of experimental setup. Because of that, the microgravity conditions in orbital research laboratories provide ideal means for investigating transport processes due to the absence or significant suppression of gravitational convection [6]. The factors described above justify the necessity of space experiments.

In 2013, the ESA Topical team "Diffusion in nonmetallic liquids" decided to perform the Benchmark on the mass transport coefficient measurements in ternary mixtures. The goal of this Benchmark is to provide the values of mass transport coefficients measured in ground laboratories and compare them with those obtained in DCMIX 1 experiment on the International Space Station (ISS). The teams from Mondragon Goi Eskola Politeknikoa, Spain, Ryerson University, Toronto, Canada, Université Libre de Bruxelles, Belgium, Universität Bayreuth, Germany, and RAS team consisting of the Institute of Continuous Media Mechanics UB RAS, Perm, Russia and Institute of Computational Modelling SB RAS, Krasnoyarsk, Russia take part in the Benchmark. The mixture chosen for the Benchmark is 1,2,3,4–tetrahydronaphthalene (THN), isobutylbenzene (IBB), and $n$-dodecane ($n\mathrm{C}_{12}$) at mass fractions of 0.8/0.1/0.1 and at 25 °C. Diffusion, thermal diffusion, and Soret coefficients have been measured in microgravity and ground conditions. The experimental techniques used in ground laboratories are: Optical beam deflection, optical digital interferometry, Taylor dispersion technique, Thermogravitational column, Sliding symmetric tubes, and Open ended capillary technique. In microgravity conditions, four teams have performed independent analysis of the measurements carried out in the SODI facility on the ISS.

The present paper describes the contribution of the RAS team to the Benchmark study. The performed data processing includes two stages: 1) obtaining the fields of refractive indices by processing raw interferometric images from DCMIX 1 experiment; 2) determining the diffusion and Soret coefficients from the temporal and spatial evolution of refractive indices.

## 2 Experimental setup

The experimental setup is based on Selectable Optical Diagnostic Instrument (SODI) installed in the Microgravity Science Glovebox on the International Space Station. The Optical digital interferometry is used to observe and record the spatiotemporal variations of composition in optically transparent mixtures.

The setup consists of an array of five Soret cells filled with different mixtures and a movable optical system able to traverse all these cells. The additional (companion) cell is probed with a fixed optical system (fig. 1). The cell array is enclosed into a thermally stabilized case. Each Soret cell consists of a rectangular glass chamber of the size 10 × 10 × 5 mm fixed between two copper plates thermally stabilized by the Peltier modules. The plates incorporate thermal registration, volume expansion compensation, and filling systems. The cells are prepared and sealed on the ground, and require no maintenance during space flight.

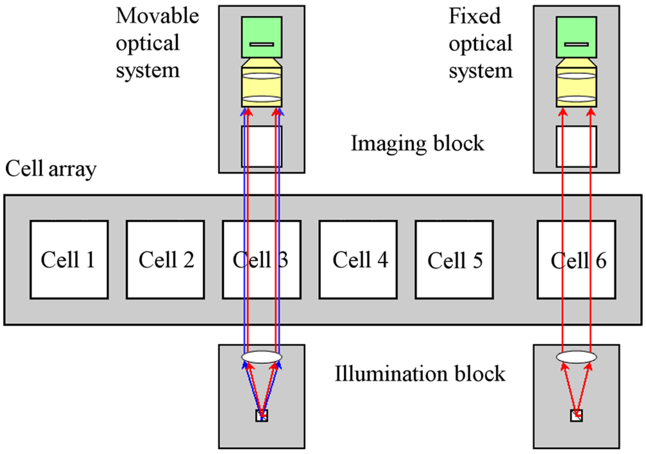

**Fig. 1.** Cell array with movable and fixed optical systems.

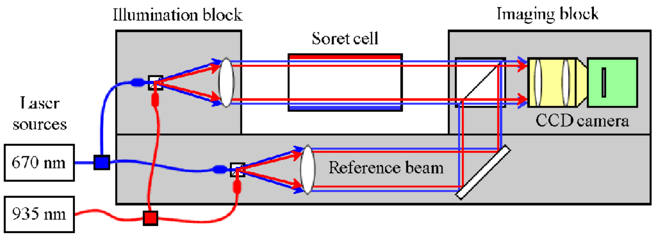

**Fig. 2.** Principle scheme of Mach-Zehnder interferometer.

The movable optical system consists of illumination and imaging blocks. It principally implements the Mach-Zehnder interferometer (fig. 2). Having equipped with two laser sources of different wavelengths (670 nm and 935 nm), this system is capable of resolving mixtures with up to three components. The fixed optical system is equipped with one laser source of 670 nm and intended for measurements in a binary mixture, which fills the companion cell.

The interferometer works as follows. The coherent beam of light emitted by the selected laser source is first expanded by the collimation device to form a beam with the size large enough to cover the entire frontal projection of the experimental cell. Then the beam is split into two beams by the splitter made of half-silvered mirror. The resulting beams, namely the reference beam and the sample beam, follow distinct paths before getting recombined in another beam splitter right before the imaging device. The reference beam goes through the thermally stabilized air and experiences two reflections on the mirrors along its way. The sample beam goes straight through the selected Soret cell capturing optical inhomogeneities caused by temperature and concentration variations as well as other factors. The imaging block comprises an optical system followed by a CCD camera, which produces full HD grayscale images. The camera captures and transfers the resulting interference images to the computer. The latter is also used as a storage device.

The entire SODI facility is fully programmable, and thus requires minimal interference from the ISS personnel. The program controls various aspects of the experimental

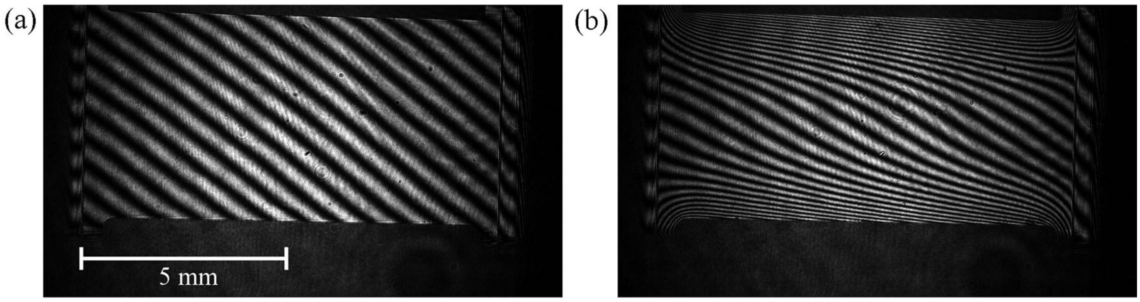

**Fig. 3.** Interference images corresponding to homogeneous (a) and non-homogeneous (b) temperature and concentration fields.

runs including the Peltier modules on/off times, movable optical system repositioning, Soret cell and laser beam selection, image capturing, and storage. The facility also performs extensive logging by collecting and writing the telemetry information covering global timings, instant temperature readings inside copper plates around the Soret cells, Peltier modules power consumption, etc. The recorded data array was available on the ground after completion of the entire experimental session upon return of the ISS mission.

The experiment is performed in two steps. First, the temperature gradient is applied to the thermally stabilized mixture. The separation of the mixture by thermal diffusion continues until the stationary state is reached (the Soret step). After that, the temperature gradient is removed and the mixture becomes isothermal. Then it is gradually homogenized by diffusion (the Diffusion step).

## 3 Data processing

### 3.1 Processing of interferometric images

The mixture THN/IBB/$n\mathrm{C}_{12}$ with mass fractions 0.8/0.1/0.1 was contained in Cell 3 of the cell array. The measurements in Cell 3 were repeated 6 times in experimental Runs with numbers 3, 8, 13, 18, 23, 28, which were performed on the ISS in December 2011 - January 2012. It was found that Run 13 suffered from a significant loss of data due to poor quality of optical images, which did not allow us to extract the values of transport coefficients. The other runs were processed successfully.

The interference patterns came as raw 8-bit grayscale images of size $1920 \times 1080$. They were grouped in .stk files by five consecutive images taken within one second. The exact number of images varied with the runs. For example, Run 3 contained 1875 images for the laser beam with the wavelength of $\lambda = 670\,\mathrm{nm}$ (herein referred to as MR) and 1880 images for the laser beam with the wavelength of $\lambda = 935\,\mathrm{nm}$ (herein referred to as MN). These images covered approximately 15 hours of experimental time. The first images in the MR/MN sequence corresponded to the moment right before the temperature difference was applied. After skipping consecutive images taken within one second interval, the filtered image set contained 686 MR images and 727 MN images.

In order to recover the continuous optical phase field and subsequently the refractive indices from interference images, the latter were subjected to the widely known two-dimensional Fourier filtering method [7, 8]. This method allows to reconstruct optical phase from a single interference image in contrast to another widely employed method, the phase-shifting interferometry [9, 10], which requires a series of interference images to produce a single optical phase field.

Two sample interference images for the MR laser are presented in fig. 3. The first image (a) represents initial state with homogeneous temperature and concentration fields. In this case, optically visible inhomogeneity in the form of equidistant inclined stripes is induced within the interferometer system itself. The frequency of these stripes is known as the carrier frequency. It plays the crucial role in processing method as clarified below. The remaining visible artifacts are due to non-ideality of optical system and experimental cell. The second image (b) corresponds to some instant after the temperature difference was applied between the top and bottom walls of the cell. It can be seen that the initially ideal stripe pattern gets curved to reflect the effect of temperature and concentration inhomogeneity on optical phase field in the direction normal to the view plane.

#### 3.1.1 Forward Fourier transform

The forward two-dimensional real-to-complex Fourier transformation of source image $f$ in the spatial domain $(x, z)$ (see samples in fig. 3) yields the image spectrum $F$ in the frequency domain $(u, w)$:

$$F(u,w) = \int_{-\infty}^{\infty} \int_{-\infty}^{\infty} f(x,z)\, e^{-2\pi i (xu+zw)}\, \mathrm{d}x\, \mathrm{d}z. \qquad (1)$$

In order to speed up the computation of (1), a discrete form of the algorithm known as Fast Fourier Transform (FFT) was employed.

#### 3.1.2 Quadrants exchange

In the image spectrum resulted from the forward Fourier transform of the source interference pattern (step 3.1.1), the meaningful data is located in disjoint corner areas.

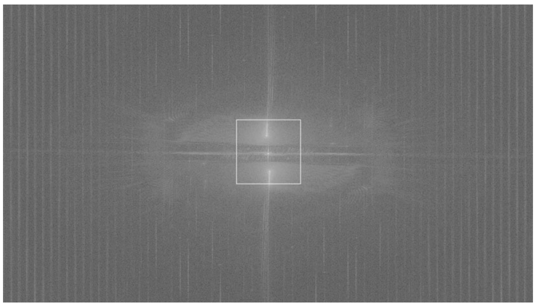

**Fig. 4.** Power spectrum of frequency domain. The rectangle depicts a general area of interest.

The quadrants exchange operation is employed in order to join the meaningful frequency data subdomains and group them around the center of frequency domain. Figure 4 represents the logarithmic view of power spectrum of frequency domain corresponding to the sample image shown in fig. 3(b) after forward Fourier transform and quadrants exchange operations.

### 3.1.3 Bandpass filtering

The image spectrum obtained at step 3.1.2 contains two identical areas symmetrically aligned around the center of domain and separated by the carrier frequency. Each area holds complete information about the phase, therefore we are free to use the either one. In our case, it is the upper area. By employing the bandpass filtering, we select the rectangular window, which covers the area of interest and zero out its exterior. The window's size and position are determined visually from the logarithmic view of power spectrum image (see fig. 5). The window of choice is meant to cover sufficient frequency range and is centered around the local maximum of power spectrum (note the oval area in fig. 5). It was found that the most suitable power spectrum image for obtaining the window's parameters is the one coming from the interferometric image of the last part of Soret step ($t > 10^4$ s), where the frequency range is maximal. The window picked this way is then employed for bandpass filtering of the entire MN/MR image sequence.

### 3.1.4 Carrier frequency removal

The carrier frequency introduced by a tilted mirror within the Mach-Zehnder interferometer manifests itself as a set of equidistant strips on an unperturbed interferometric image (see *e.g.* fig. 3(a)). This frequency can be easily determined by applying steps 3.1.1-3.1.2 to this image. The obtained power spectrum has two outstanding maxima $(u^1, w^1)$ and $(u^2, w^2)$ symmetrically aligned around the center of domain $(u_0, w_0)$. The selected maximum $(u^*, w^*)$ must correspond to the side of the area selected at step 3.1.3. The sample maximum is depicted as a cross in fig. 5.

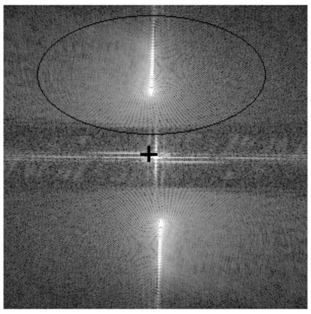

**Fig. 5.** Excerpt of power spectrum from fig. 4. The eligible area for the bandpass filtering is shown by the oval. The carrier frequency position $(u^*, w^*)$ is marked by the cross.

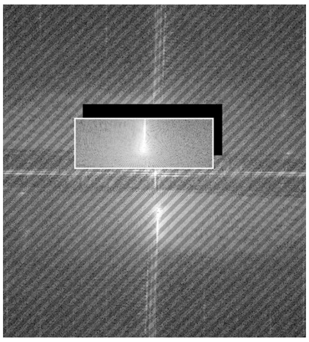

**Fig. 6.** Bandpass filtering and carrier frequency removal.

The carrier frequency removal is performed by shifting the entire filtered MN/MR spectra resulting from step 3.1.3 by $(u^* - u_0, w^* - w_0)$ pixels. Figure 6 shows combined effect of applying bandpass filtering and carrier frequency removal to fig. 4. The surviving part of the spectrum is highlighted; the rest is to be zeroed out.

### 3.1.5 Inverse Fourier transform

The inverse two-dimensional complex-to-complex Fourier transformation is applied to the filtered image spectrum

$$f(x,z) = \int_{-\infty}^{\infty}\int_{-\infty}^{\infty} F(u,w)\, e^{2\pi i(xu+zw)}\, \mathrm{d}u\, \mathrm{d}w. \qquad (2)$$

It gives the complex form of the interference image stripped of the carrier frequency. The inverse mode of FFT algorithm is employed. Note that $f$ in (2) is a complex field with both real and imaginary parts containing meaningful information.

### 3.1.6 Wrapped phase reconstruction

The wrapped optical phase $\phi$ is reconstructed from $f$ as follows:

$$\phi = \arctan \frac{\mathrm{Im}\, f}{\mathrm{Re}\, f}\,. \qquad (3)$$

Figure 7 shows the result of the wrapped phase reconstruction from the sample image in fig. 3(b).

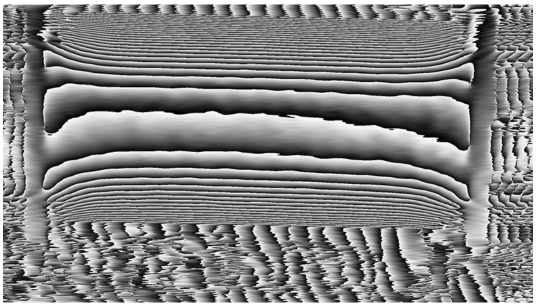

**Fig. 7.** Wrapped optical phase image.

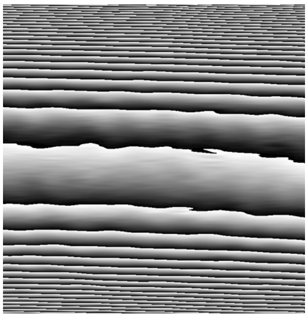

**Fig. 8.** Cropped part of optical phase image.

### 3.1.7 Wrapped phase cropping

Phase image cropping is performed to remove unwanted cell interior captured by the camera as well as phase inhomogeneities near the sidewalls. The cropped parts capture the central area of the cells in horizontal direction and span approximately half of the distance between the cell side walls. In the vertical direction, the cropping starting and ending points were symmetrically offset from the heated/cooled boundaries by a few pixels as the boundary errors were found to be the main source of errors for the resulting refractive indices. The vertical size of the cropped part was 4.9 mm in contrast to the full distance between the heaters of 5.0 mm. The cropped part of fig. 7, which contains the relevant information, is shown in fig. 8.

### 3.1.8 Subtraction of reference wrapped phase

To determine the phase change induced by concentration variations only, the reference wrapped phase $\phi_0$ is selected. This wrapped phase corresponds to the reference image with homogeneous temperature field (for the Diffusion step) or with linear temperature field (for the Soret step). The reference wrapped phase $\phi_0$ is subtracted from the current wrapped phase $\phi$. This procedure is applied to all interference images in the MR/MN sequence. In what follows, it will be referred to as subtraction of reference image.

### 3.1.9 Phase unwrapping

Due to the nature of inverse tangent, the field values obtained from (3) are limited to the interval $[-\pi, \pi)$. However, the real optical phase is known to be continuous and it can extend over this range. In order to remove the discontinuities, the process known as the phase unwrapping is employed. The principal equation of phase unwrapping is as follows:

$$(\phi - \phi_0) + 2\pi k = \Delta\varphi, \tag{4}$$

where $\Delta\varphi$ is the unwrapped optical phase difference and $k$ is an integer. The problem reduces to the determination of the right number $k$. Figure 9 shows the result of unwrapping of fig. 8.

**Fig. 9.** Unwrapped optical phase image.

In general, phase unwrapping is a non-trivial task, especially for distorted wrapped images, for which the direct application of eq. (4) yields unsatisfactory results [9]. However, as the resulting wrapped optical phases in our case are of sufficient quality (see fig. 8), the phase fringes exhibit a strict horizontal alignment. Since we are interested in the optical phase difference between different positions in the vertical direction, a one-dimensional sequential phase unwrapper in vertical direction has been employed. The resulting vertical profile of the unwrapped phase was selected from a full set of vertical profiles corresponding to different values of the horizontal coordinate, see fig. 9. The selected profile is characterized by the minimal presence of residual phase discontinuities, which are considered erroneous due to the smooth nature of the presumed profile.

### 3.1.10 Refractive index reconstruction

Finally, the refractive index difference is computed by applying the following formula

$$\Delta n(x,z) = \frac{\lambda}{2\pi L_y}\Delta\varphi(x,z)$$

to the unwrapped optical phase difference $\Delta\varphi$ from (4). Here $\lambda$ is the corresponding wavelength and $L_y$ is the optical path in liquid in the $y$-direction normal to the view plane, see fig. 10. The refractive index profiles are computed simultaneously for MN and MR images.

## 3.2 Determination of transport coefficients

In this section, we describe the method for extracting diffusion, thermal diffusion, and Soret coefficients from the

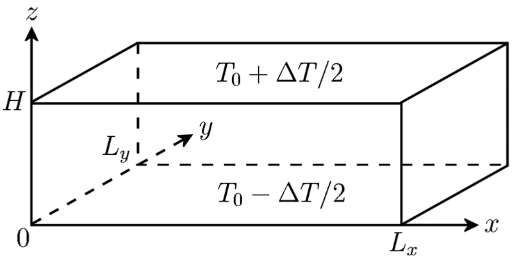

**Fig. 10.** Geometry of the experimental cell.

evolution of refractive index in the experimental cell. This method was originally developed for optical beam deflection setup in [11]. In this work, we extend it to optical digital interferometry and take into account not only the temporal variation of refractive index, but also its profile along the diffusion path.

Let us consider a mixture with $N$ components, which composition is given by $\boldsymbol{C} = (C_1, \ldots, C_{N-1})^T$, where $^T$ denotes the transpose (in this case, a column vector). In the three-dimensional space $x, y, z$, the diffusive fluxes of components in the $z$ direction $\boldsymbol{J}_z = (J_{z1}, \ldots, J_{z,N-1})^T$ are written as

$$\boldsymbol{J}_z = -\rho D \frac{\partial \boldsymbol{C}}{\partial z} - \rho \boldsymbol{D_T} \frac{\partial T}{\partial z}\,. \tag{5}$$

Similar expressions are valid for $x$ and $y$ directions. Here $T$ is the temperature, $D$ is the square matrix of $(N-1)^2$ diffusion coefficients $D_{ij}$, $\boldsymbol{D_T} = (D_{T1}, \ldots, D_{T,N-1})^T$ is the vector of thermal diffusion coefficients, and $\rho$ is the constant density of the mixture.

In the experiment, the mixture is placed in a rectangular cell with height $H$ (fig. 10). Initially, the mixture is isothermal and homogeneous, *i.e.* $T = T_0$, $\boldsymbol{C} = \boldsymbol{C}_0 = (C_{01}, \ldots, C_{0,N-1})^T$. Then the temperature difference $\Delta T$ is applied between the top and bottom walls. As a result, the temperature gradient appears and causes the concentration gradient due to the Soret effect. Assuming that the heat and mass transfer occur in the $z$-direction only, the governing equations and imposed conditions can be written as

$$\frac{\partial T}{\partial t} = \chi \frac{\partial^2 T}{\partial z^2}\,, \tag{6}$$

$$T(0,z) = T_0, \qquad T(t,0) = T_0 - \frac{\Delta T}{2}\,,$$
$$T(t,H) = T_0 + \frac{\Delta T}{2}\,, \tag{7}$$

$$\frac{\partial \boldsymbol{C}}{\partial t} = D \frac{\partial^2 \boldsymbol{C}}{\partial z^2} + \boldsymbol{D_T} \frac{\partial^2 T}{\partial z^2}\,, \tag{8}$$

$$\begin{aligned} &\boldsymbol{C}(0,z) = \boldsymbol{C}_0, \\ &D \frac{\partial \boldsymbol{C}}{\partial z}(t,0) + \boldsymbol{D_T} \frac{\partial T}{\partial z}(t,0) = \\ &\qquad D \frac{\partial \boldsymbol{C}}{\partial z}(t,H) + \boldsymbol{D_T} \frac{\partial T}{\partial z}(t,H) = 0. \end{aligned} \tag{9}$$

Here $\chi$ is the thermal diffusivity. When the stationary state is reached, the temperature and concentration profiles become linear in $z$ coordinate:

$$\begin{aligned} T &= T_s \equiv T_0 + \Delta T \left( \frac{z}{H} - \frac{1}{2} \right), \\ \boldsymbol{C} &= \boldsymbol{C}_s \equiv \boldsymbol{C}_0 - D^{-1} \boldsymbol{D_T} \Delta T \left( \frac{z}{H} - \frac{1}{2} \right). \end{aligned} \tag{10}$$

The separation of components induced by the temperature gradient occurs during the Soret step of the experiment. It is followed by the diffusion step, in which the temperature difference is removed by setting the wall temperatures to $T = T_0$. With time, the mixture becomes isothermal, and concentration gradients gradually diffuse to homogeneous state. This process is described by eqs. (6) and (8), while the imposed conditions are given by

$$\begin{aligned} &T(0,z) = T_s, \qquad T(t,0) = T(t,H) = T_0, \\ &\boldsymbol{C}(0,z) = \boldsymbol{C}_s, \end{aligned} \tag{11}$$

$$\begin{aligned} &D \frac{\partial \boldsymbol{C}}{\partial z}(t,0) + \boldsymbol{D_T} \frac{\partial T}{\partial z}(t,0) = \\ &\qquad D \frac{\partial \boldsymbol{C}}{\partial z}(t,H) + \boldsymbol{D_T} \frac{\partial T}{\partial z}(t,H) = 0. \end{aligned} \tag{12}$$

In liquid mixtures, the heat transfer by conduction occurs much faster than the mass transfer by diffusion. The ratio of diffusion time to the thermal time has the order of 100. In this case, the description of Soret step can be simplified by assuming that the linear temperature profile (10) is already established before the separation starts. The diffusion step, in its turn, is supposed to occur in a completely isothermal mixture. These assumptions are violated for small times, where the heat and mass transfer occur simultaneously. This case will be considered in more detail later. Under the above assumptions, problems (8), (9) describing the Soret step can be rewritten as

$$\begin{aligned} &\frac{\partial \boldsymbol{C}}{\partial t} = D \frac{\partial^2 \boldsymbol{C}}{\partial z^2}\,, \qquad \boldsymbol{C}(0,z) = \boldsymbol{C}_0, \\ &\frac{\partial \boldsymbol{C}}{\partial z}(t,0) = \frac{\partial \boldsymbol{C}}{\partial z}(t,H) = \frac{\boldsymbol{\Delta C}_s}{H}\,, \end{aligned} \tag{13}$$

where

$$\begin{aligned} \boldsymbol{\Delta C}_s = (\Delta C_{s1}, \ldots, \Delta C_{s,N-1})^T &\equiv \boldsymbol{C}_s(H) - \boldsymbol{C}_s(0) \\ &= -D^{-1} \boldsymbol{D_T} \Delta T \end{aligned} \tag{14}$$

is the vector of concentration differences between the top and bottom walls at the stationary state, see (10). Equations (8) and conditions (12) for the Diffusion step are reduced to

$$\begin{aligned} &\frac{\partial \boldsymbol{C}}{\partial t} = D \frac{\partial^2 \boldsymbol{C}}{\partial z^2}\,, \qquad \boldsymbol{C}(0,z) = \boldsymbol{C}_s, \\ &\frac{\partial \boldsymbol{C}}{\partial z}(t,0) = \frac{\partial \boldsymbol{C}}{\partial z}(t,H) = 0. \end{aligned} \tag{15}$$

To solve (13) and (15), we diagonalize the diffusion matrix by the transformation $\Lambda = P^{-1} D P$. Here $P$ is the matrix, whose columns are eigenvectors of $D$, and

$\Lambda = \mathrm{diag}\{\lambda_1, \dots, \lambda_{N-1}\}$ is the diagonal matrix of eigenvalues. By introducing new concentrations $\boldsymbol{W} = P^{-1}\boldsymbol{C}$, problem (13) is reduced to

$$\begin{aligned} &\frac{\partial \boldsymbol{W}}{\partial t} = \Lambda \frac{\partial^2 \boldsymbol{W}}{\partial z^2}, \qquad \boldsymbol{W}(0,z) = \boldsymbol{W}_0, \\ &\frac{\partial \boldsymbol{W}}{\partial z}(t,0) = \frac{\partial \boldsymbol{W}}{\partial z}(t,H) = \frac{\Delta \boldsymbol{W}_s}{H}, \end{aligned} \tag{16}$$

where $\boldsymbol{W}_0 = P^{-1}\boldsymbol{C}_0$ and

$$\Delta \boldsymbol{W}_s = P^{-1}\Delta \boldsymbol{C}_s = (\Delta W_{s1}, \dots, \Delta W_{s,N-1})^T. \tag{17}$$

The application of the same procedure to problem (15) gives

$$\begin{aligned} &\frac{\partial \boldsymbol{W}}{\partial t} = \Lambda \frac{\partial^2 \boldsymbol{W}}{\partial z^2}, \qquad \boldsymbol{W}(0,z) = \boldsymbol{W}_s, \\ &\frac{\partial \boldsymbol{W}}{\partial z}(t,0) = \frac{\partial \boldsymbol{W}}{\partial z}(t,H) = 0, \end{aligned} \tag{18}$$

where $\boldsymbol{W}_s = P^{-1}\boldsymbol{C}_s$. Since the matrix $\Lambda$ is diagonal, each of the problems (16) and (18) represents a set of $N-1$ independent equations and imposed conditions, which can be solved by the separation of variables [12] in the same way as for binary mixture [13]. The solution of both problems can be written in the universal form

$$\boldsymbol{W} = \boldsymbol{W}_0 + V\boldsymbol{w}, \tag{19}$$

where

$$V = \mathrm{diag}\{\Delta W_{s1}, \dots, \Delta W_{s,N-1}\} \tag{20}$$

is the diagonal matrix and $\boldsymbol{w}(t,z) = (w_1, \dots, w_{N-1})^T$ is the vector of functions. For the Soret step (problem (16)), these functions are given by

$$\begin{aligned} w_j(t,z) = {} & \frac{z}{H} - \frac{1}{2} + \frac{4}{\pi^2}\sum_{k=0}^{\infty}\frac{1}{(2k+1)^2} \\ & \times \cos\left(\frac{(2k+1)\,\pi z}{H}\right)\exp\left(-(2k+1)^2\,\frac{t}{\tau_j}\right), \end{aligned}$$

while for the Diffusion step (problem (18)) they have the form

$$\begin{aligned} w_j(t,z) = {} & -\frac{4}{\pi^2}\sum_{k=0}^{\infty}\frac{1}{(2k+1)^2} \\ & \times \cos\left(\frac{(2k+1)\,\pi z}{H}\right)\exp\left(-(2k+1)^2\,\frac{t}{\tau_j}\right), \end{aligned}$$

where $\tau_j = H^2/\pi^2\lambda_j$ are the relaxation times for diffusion, $j = 1, \dots, N-1$.

In what follows, we will need the concentration differences between symmetric points with respect to the mid–height of the cell:

$$\begin{aligned} &\Delta \boldsymbol{W}(t,z') \equiv \boldsymbol{W}\left(t, \frac{H}{2} + z'\right) - \boldsymbol{W}\left(t, \frac{H}{2} - z'\right) = \\ &V\Delta \boldsymbol{w}(t,z') = V\left(\boldsymbol{w}\left(t, \frac{H}{2} + z'\right) - \boldsymbol{w}\left(t, \frac{H}{2} - z'\right)\right), \end{aligned} \tag{21}$$

where $\Delta \boldsymbol{w}(t,z') = (\Delta w_1, \dots, \Delta w_{N-1})^T$, $0 \leqslant z' \leqslant H/2$, and (19) was used. For the Soret step, one has

$$\begin{aligned} \Delta w_j(t,z') = {} & \frac{2z'}{H} - \frac{8}{\pi^2}\sum_{k=0}^{\infty}\frac{(-1)^k}{(2k+1)^2}\sin\left(\frac{(2k+1)\,\pi z'}{H}\right) \\ & \times \exp\left(-(2k+1)^2\,\frac{t}{\tau_j}\right), \end{aligned} \tag{22}$$

while for the Diffusion step

$$\begin{aligned} \Delta w_j(t,z') = {} & \frac{8}{\pi^2}\sum_{k=0}^{\infty}\frac{(-1)^k}{(2k+1)^2}\sin\left(\frac{(2k+1)\,\pi z'}{H}\right) \\ & \times \exp\left(-(2k+1)^2\,\frac{t}{\tau_j}\right), \end{aligned} \tag{23}$$

where $j = 1, \dots, N-1$. The concentration differences in the original variables are found from

$$\Delta \boldsymbol{C}(t,z') = P\Delta \boldsymbol{W}(t,z'). \tag{24}$$

To experimentally observe the evolution of composition with time, the Optical digital interferometry can be employed. For a mixture with $N$ components, $N-1$ laser beams of different wavelengths are required. These beams traverse the entire cell perpendicular to the temperature gradient (in $y$-direction, see fig. 10). Both thermal and compositional fields contribute to the temporal and spatial evolution of refractive indices $\boldsymbol{n}(t,z) = (n_1, \dots, n_{N-1})^T$. The thermal contribution can be eliminated by taking the reference image at the time when linear (homogeneous) temperature field is established in the case of Soret (Diffusion) step. This reference image is then subtracted from all subsequent images.

The difference of refractive indices between symmetric points with respect to the mid-height of the cell is given by

$$\begin{aligned} \Delta \boldsymbol{n}(t,z') &\equiv \boldsymbol{n}\left(t, \frac{H}{2} + z'\right) - \boldsymbol{n}\left(t, \frac{H}{2} - z'\right) \\ &= \frac{\partial \boldsymbol{n}}{\partial \boldsymbol{C}}\,\Delta \boldsymbol{C}(t,z'). \end{aligned} \tag{25}$$

Here $\partial \boldsymbol{n}/\partial \boldsymbol{C}$ is the matrix of contrast factors, *i.e.* refractive indices derivatives with respect to concentrations $\partial n_i/\partial C_j$, $i,j = 1, \dots, N-1$. This matrix will be denoted by $N_C$. With the help of (21) and (24), eq. (25) can be transformed into

$$\begin{aligned} \Delta \boldsymbol{n}(t,z') &= N_C\Delta \boldsymbol{C}(t,z') = N_C P P^{-1}\Delta \boldsymbol{C}(t,z') \\ &= N_C P\Delta \boldsymbol{W}(t,z') = K\Delta \boldsymbol{w}(t,z'), \end{aligned}$$

where the matrix $K = N_C P V$ was introduced. The matrix $K$ and the eigenvalue matrix $\Lambda$ can be found from the regression analysis of relation

$$\Delta \boldsymbol{n}(t,z') = K\Delta \boldsymbol{w}(t,z'). \tag{26}$$

Here the left-hand side is measured experimentally, while the vector on the right-hand side represents the analytical solution given by (22) and (23) for the Soret and diffusion steps, respectively. Before proceeding to regression analysis, let us provide formulas for calculating diffusion and thermal diffusion coefficients from the known $K$ and $\Lambda$. Note that the matrix $U = PV = N_C^{-1}K$ is also an eigenvector matrix of $D$. The effect of multiplying $P$ by a diagonal matrix $V$ is only to change the magnitude of each eigenvector. Then the matrix of diffusion coefficients is given by

$$D = U\Lambda U^{-1}, \qquad U = N_C^{-1}K. \tag{27}$$

The thermal diffusion coefficients are found from (14) with the help of (17) and (20):

$$\begin{aligned}\Delta T \boldsymbol{D_T} &= -D\Delta\boldsymbol{C}_s = -P\Lambda P^{-1}\Delta\boldsymbol{C}_s\\ &= -UV^{-1}\Lambda VV^{-1}\Delta\boldsymbol{W}_s = -U\Lambda\boldsymbol{I},\end{aligned}$$

where $\boldsymbol{I} = (1,\ldots,1)^T$. It follows that

$$\boldsymbol{D_T} = -\frac{1}{\Delta T}U\Lambda\boldsymbol{I}. \tag{28}$$

Taking into account the definition of the Soret coefficients $\boldsymbol{S_T} = (S_{T1},\ldots,S_{TN-1})^T$ (see (5))

$$\frac{\partial\boldsymbol{C}}{\partial z} = -\boldsymbol{S_T}\frac{\partial T}{\partial z}, \qquad \boldsymbol{S_T} = D^{-1}\boldsymbol{D_T},$$

from (27) and (28) we find

$$\boldsymbol{S_T} = -\frac{1}{\Delta T}U\boldsymbol{I}. \tag{29}$$

We now turn to the regression procedure, which allows finding $K$ and $\Lambda$ from eq. (26). Let the differences of refractive indices be measured experimentally at time moments $t = t_m$, $m = 1,\ldots,M$ and positions $z' = z'_r$, $r = 1,\ldots,R$. Using the notation $\Delta n_{imr} \equiv \Delta n_i(t_m, z'_r)$ and $\Delta w_{jmr} \equiv \Delta w_j(t_m, z'_r)$, we can rewrite (26) as

$$\begin{aligned}&\Delta n_{imr} = \sum_{j=1}^{N-1} K_{ij}\Delta w_{jmr},\\ &i = 1,\ldots,N-1,\ m = 1,\ldots,M,\ r = 1,\ldots,R.\end{aligned} \tag{30}$$

The least squares method is used to find the elements $K_{ij}$. The sum of squared errors for beam $i$ is

$$E_i = \sum_{r=1}^{R}\sum_{m=1}^{M}\left(\sum_{j=1}^{N-1}K_{ij}\Delta w_{jmr} - \Delta n_{imr}\right)^2. \tag{31}$$

For a given set of eigenvalues $\lambda_j$, this sum reaches a minimum when all derivatives $\partial E_i/\partial K_{ik} = 0$:

$$\begin{aligned}\frac{\partial E_i}{\partial K_{ik}} &= 2\sum_{r=1}^{R}\sum_{m=1}^{M}\left(\sum_{j=1}^{N-1}K_{ij}\Delta w_{jmr} - \Delta n_{imr}\right)\\ &\quad\times\Delta w_{kmr} = 0, \quad k = 1,\ldots,N-1.\end{aligned} \tag{32}$$

Let us introduce matrices $N_r = \{\Delta n_{imr}\}$ and $W_r = \{\Delta w_{jmr}\}$ with the dimension $(N-1)\times M$. Then relations (32) can be written in a compact form

$$\sum_{r=1}^{R}(KW_r - N_r)\,W_r^T = 0,$$

where $W_r^T$ is the transpose of $W_r$. Solving the above equation with respect to $K$ gives

$$K = \left(\sum_{r=1}^{R}N_rW_r^T\right)\left(\sum_{r=1}^{R}W_r\,W_r^T\right)^{-1}.$$

With the matrix $K$ given by this formula, the total sum of squared errors,

$$E = E_1 + \ldots + E_{N-1}, \tag{33}$$

is a function of eigenvalues $\lambda_j$ only. They can be found by numerical minimization of $E$. In this work, we use the Nelder-Mead method [14]. The initial approximation of eigenvalues can be obtained by estimating the relaxation times $\tau_j = H^2/\pi^2\lambda_j$ from the time evolution of the measured refractive index differences $\Delta n_i(t, H/2)$ between the top and bottom walls of the cell.

Let us now return to the assumption that the linear temperature profile (see (10)) is already established before the Soret separation begins. In reality, the separation starts along with the build-up of temperature gradient. By the time when the temperature profile is formed, there is already some separation near the top and bottom walls. A simple way to correct for this separation was proposed in [3]. Suppose that the reference image is taken at time $t = t_0$ from the start of the experiment when the temperature profile is completely established. In this case, relation (25) can be corrected as follows:

$$\Delta\boldsymbol{n}(t,z') = \frac{\partial\boldsymbol{n}}{\partial\boldsymbol{C}}\left(\Delta\boldsymbol{C}(t_0+t,z') - \Delta\boldsymbol{C}(t_0,z')\right).$$

Then the following equation

$$\Delta\boldsymbol{n}(t,z') = K\left(\Delta\boldsymbol{w}(t_0+t,z') - \Delta\boldsymbol{w}(t_0,z')\right) \tag{34}$$

must be used instead of eq. (26) in the regression analysis for the Soret step. For the diffusion step, the reference image corresponds to the isothermal state, which is reached at time $t = t_0$ after setting the same temperatures at top and bottom walls. In this case, eq. (26) must be modified as follows:

$$\Delta\boldsymbol{n}(t,z') = K\Delta\boldsymbol{w}(t_0+t,z'). \tag{35}$$

The initial separation can be calculated precisely by solving heat transfer problem (6), (7) and using the obtained solution to solve mass transfer problem (8), (9). However, the absence of a simple analytical solution for the concentration fields in this case would make the regression analysis complicated and time consuming.

**Table 1.** Eigenvalues of diffusion matrix, diffusion, thermal diffusion, and Soret coefficients for ternary mixture $n\mathrm{C}_{12}$ (1), IBB (2), THN (3) with equal mass fractions 1/3 at 25 °C [16].

| $\lambda_1$ | $\lambda_2$ | $D_{11}$ | $D_{12}$ | $D_{21}$ | $D_{22}$ | $D'_{T1}$ | $D'_{T2}$ | $S_{T1}$ | $S_{T2}$ |
|---|---|---|---|---|---|---|---|---|---|
| $10^{-10}$ m$^2$/s | | $10^{-10}$ m$^2$/s | | | | $10^{-12}$ m$^2$/s K | | $10^{-3}$ 1/K | |
| 6.81 | 11.00 | 6.70 | 0.43 | −1.08 | 11.10 | −0.81 | −0.93 | −1.15 | −0.95 |

**Table 2.** Contrast factor matrices used in the test calculations. Matrix 1 is taken from [16] and corresponds to the lasers with wavelengths 633 nm (1) and 405 nm (2) for ternary mixture $n\mathrm{C}_{12}$ (1), IBB (2), THN (3) with equal mass fractions 1/3 at 25 °C.

| Matrix | $\partial n_1/\partial C_1$ | $\partial n_1/\partial C_2$ | $\partial n_2/\partial C_1$ | $\partial n_2/\partial C_2$ | Condition number $\mathcal{K}$ |
|---|---|---|---|---|---|
| 1 | −0.1201 | −0.0495 | −0.1431 | −0.0475 | 29 |
| 2 | −0.1428 | −0.0487 | −0.1431 | −0.0475 | 245 |

The Soret coefficients can be determined not only from transient state, but also from the stationary state. It follows from (26) that the difference of refractive indices between the top and bottom walls at the stationary state is given by

$$\boldsymbol{\Delta n}_s \equiv \boldsymbol{\Delta n}(\infty, H/2) = K\boldsymbol{\Delta w}(\infty, H/2) = K\boldsymbol{I}. \qquad (36)$$

With a help of (29) and (36), the Soret coefficients can be expressed via $\boldsymbol{\Delta n}_s$

$$\boldsymbol{S_T} = -\frac{1}{\Delta T} N_C^{-1} \boldsymbol{\Delta n}_s. \qquad (37)$$

For reliable determination of transport coefficients from formulas (27)-(29), (37), the contrast factor matrix $N_C = \partial \boldsymbol{n}/\partial \boldsymbol{C}$ must be well conditioned. Otherwise, small errors in the elements of $K$ will result in large errors in the elements of $U$ and, correspondingly, in the transport coefficients. The conditioning of an arbitrary matrix $A$ is characterized by the condition number $\mathcal{K}$, which can be calculated as [15]

$$\mathcal{K} = \left(\frac{|\lambda_{\max}|}{|\lambda_{\min}|}\right)^{1/2}, \qquad (38)$$

where $\lambda_{\max}$ and $\lambda_{\min}$ are the maximal and minimal (by moduli) eigenvalues of the matrix $A^T A$ (provided that $L_2$ norm is used). The smaller is the condition number, the less error amplification is expected after multiplying $A^{-1}$ by the input data (vector or matrix).

## 4 Validation of the method

To validate the proposed method for extracting the transport coefficients from the experimental data, we have performed tests with ternary mixture of $n\mathrm{C}_{12}$ (1), IBB (2), THN (3) with equal mass fractions (1/3). The diffusion, thermal diffusion, and Soret coefficients for this mixture were measured by optical beam deflection technique in [16]. To follow the notation of the latter work, the thermal diffusion coefficients are denoted by $D'_{Ti}$ instead of $D_{Ti}$, $i = 1, 2$. The obtained values are presented in table 1. Two laser beams with wavelengths of 633 nm (1) and 405 nm (2) were used. The corresponding contrast factors are given in table 2 (see Matrix 1 with condition number 29). To provide additional testing of the method, we have also used Matrix 2 with much higher condition number of 245. The latter was obtained from the former by changing the derivatives of $n_1$ with respect to $C_1$ and $C_2$. The temperature derivatives of refractive indices are $\partial n_1/\partial T = -4.574 \times 10^{-4}$ and $\partial n_2/\partial T = -4.892 \times 10^{-4}$ [16].

The input data for the tests were obtained on the basis of eq. (25), where the analytical solution with parameters given in tables 1 and 2 was used. The applied temperature difference was $\Delta T = 10$ K. The normally distributed random noise with the standard deviation of $\sigma_{\Delta n} = 5 \times 10^{-6}$ and zero mean was added to the refractive index curves. This noise can be associated with the typical temperature deviation $\delta T = 0.01$ K from the prescribed values at the top and bottom walls, and, correspondingly, from the linear profile in the experimental cell [3]. It leads to the deviation of refractive index $\delta n = (\partial n/\partial T)\, \delta T = 5 \times 10^{-6}$, where we put $\partial n/\partial T = 5 \times 10^{-4}$ for simplicity. The height of the cell is taken as $H = 5$ mm, so the relaxation times calculated from the eigenvalues given in table 1 are $\tau_1 = 3720$ s and $\tau_2 = 2303$ s.

The obtained curves for refractive index differences on the time interval $(0, \tau)$, where $\tau = 10\tau_1$, are shown in fig. 11(a) and (b) for contrast factor Matrices 1 and 2, respectively. The total number of sample points in time is $M = 200$ with 100 evenly distributed points on each of the intervals $(0, \tau/3)$ and $(\tau/3, \tau)$. The solid lines in fig. 11(a) correspond to the fitted analytical solution for $R = 100$ sample points in space. The curves for $\Delta n_1$ and $\Delta n_2$ are clearly separated from each other when Matrix 1 with low condition number 29 is used. The use of Matrix 2 with high condition number 245 leads to the situation when these curves almost coincide. In this case, a significant loss of precision in determination of transport coefficients can be expected.

The results of data processing are presented in tables 3 and 4 for contrast factor Matrices 1 and 2, respectively. For each number of points $R$ taken along the diffusion path, 10 runs were performed with different random noise. For any given quantity $q$, the mean value $\overline{q}$,

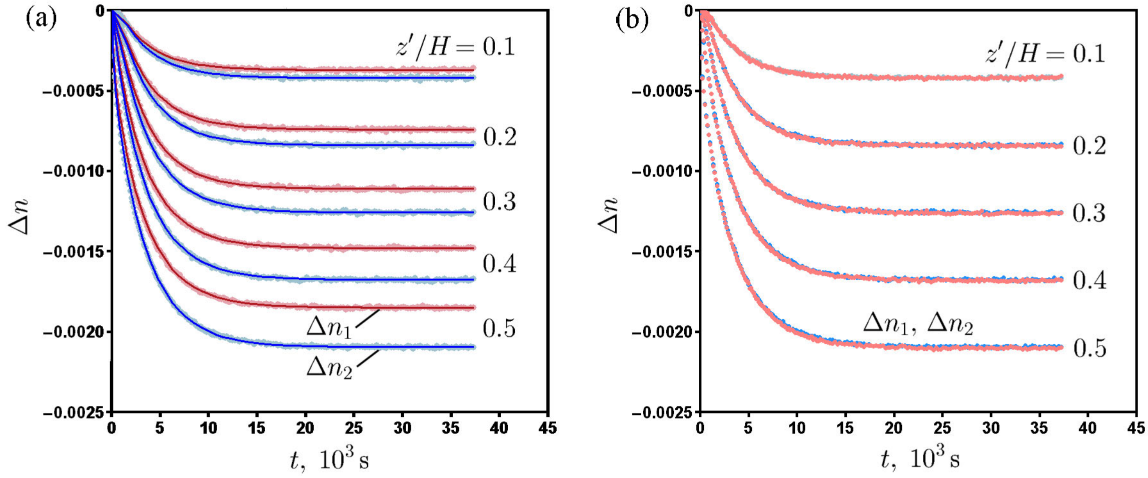

**Fig. 11.** The evolution of the differences of refractive indices $\Delta n_1$ (red) and $\Delta n_2$ (blue) with time at different positions for contrast factor Matrix 1 (a) and Matrix 2 (b). Solid lines correspond to the fitted analytical solution.

**Table 3.** Results of calculations for contrast factor Matrix 1 with $\mathcal{K} = 29$. For a given quantity $q$, $\overline{q}$ is the average value over 10 runs, $s$ is the bias-corrected standard deviation, $s/\overline{q}$ is the relative standard deviation, and $\overline{q}/q$ is the relative error with respect to the exact value $q$.

| Points | | $\lambda_1$ | $\lambda_2$ | $D_{11}$ | $D_{12}$ | $D_{21}$ | $D_{22}$ | $D'_{T1}$ | $D'_{T2}$ | $S_{T1}$ | $S_{T2}$ |
|---|---|---|---|---|---|---|---|---|---|---|---|
| $R$ | | $10^{-10}$ m$^2$/s | | | $10^{-10}$ m$^2$/s | | | $10^{-12}$ m$^2$/s K | | $10^{-3}$ 1/K | |
| 1 | $s/\overline{q}$, % | 3.1 | 10.8 | 3.3 | 87.8 | 91.8 | 10.7 | 1.2 | 3.2 | 0 | 1.1 |
| | $\overline{q}/q$, % | −0.9 | 0.3 | −0.1 | −4.7 | −9.3 | −0.1 | 0 | 1.1 | 0 | 0 |
| 10 | $s/\overline{q}$, % | 1.2 | 4.6 | 1.8 | 50 | 28.6 | 4.3 | 1.2 | 2.2 | 0 | 0 |
| | $\overline{q}/q$, % | −0.3 | −0.6 | −0.1 | −2.3 | −9.3 | −0.6 | 0 | 0 | 0 | 0 |
| 100 | $\overline{q}$ | 6.80 | 10.99 | 6.71 | 0.41 | −1.03 | 11.09 | −0.81 | −0.93 | −1.15 | −0.95 |
| | $s$ | 0.03 | 0.20 | 0.04 | 0.05 | 0.15 | 0.20 | 0 | 0.01 | 0 | 0 |
| | $s/\overline{q}$, % | 0.4 | 1.8 | 0.6 | 12.2 | 14.6 | 1.8 | 0 | 1.1 | 0 | 0 |
| | $\overline{q}/q$, % | −0.1 | −0.1 | 0.1 | −4.7 | −4.6 | −0.1 | 0 | 0 | 0 | 0 |

**Table 4.** Results of calculations for contrast factor Matrix 2 with $\mathcal{K} = 245$. For a given quantity $q$, $\overline{q}$ is the average value over 10 runs, $s$ is the bias-corrected standard deviation, $s/\overline{q}$ is the relative standard deviation, and $\overline{q}/q$ is the relative error with respect to the exact value $q$.

| Points | | $\lambda_1$ | $\lambda_2$ | $D_{11}$ | $D_{12}$ | $D_{21}$ | $D_{22}$ | $D'_{T1}$ | $D'_{T2}$ | $S_{T1}$ | $S_{T2}$ |
|---|---|---|---|---|---|---|---|---|---|---|---|
| $R$ | | $10^{-10}$ m$^2$/s | | | $10^{-10}$ m$^2$/s | | | $10^{-12}$ m$^2$/s K | | $10^{-3}$ 1/K | |
| 1 | $s/\overline{q}$, % | 3.4 | 11.9 | 115 | 348 | 386 | 162 | 8.9 | 20.8 | 1.7 | 5.3 |
| | $\overline{q}/q$, % | −1 | 0.2 | 50.9 | −1012 | −332 | −31.1 | −2.5 | 8.6 | 0 | 0 |
| 10 | $s/\overline{q}$, % | 1.5 | 5.8 | 43.2 | 231 | 207 | 19.4 | 6.3 | 13.5 | 0.9 | 3.2 |
| | $\overline{q}/q$, % | −0.6 | −1.4 | −14 | 233 | 26.9 | 6.9 | −1.2 | 3.2 | 0 | −1.1 |
| 25 | $s/\overline{q}$, % | 1 | 4.4 | 2.5 | 250 | 74.6 | 4 | 2.5 | 6.1 | 0.9 | 2.1 |
| | $\overline{q}/q$, % | 0.1 | 1.1 | 0.9 | −62.8 | −41.7 | 0.6 | −2.5 | 5.4 | 0 | 0 |
| 50 | $s/\overline{q}$, % | 0.6 | 2.5 | 1.5 | 113 | 75 | 2.5 | 1.3 | 5.2 | 0 | 1.1 |
| | $\overline{q}/q$, % | −0.1 | −0.4 | 0.6 | −44.2 | −40.7 | −0.7 | −1.2 | 4.3 | 0 | −1.1 |
| 100 | $\overline{q}$ | 6.80 | 10.99 | 6.75 | 0.27 | −0.73 | 11.05 | −0.80 | −0.96 | −1.15 | −0.94 |
| | $s$ | 0.03 | 0.22 | 0.07 | 0.19 | 0.39 | 0.22 | 0.01 | 0.03 | 0 | 0.01 |
| | $s/\overline{q}$, % | 0.4 | 2 | 1 | 70.4 | 53.4 | 2 | 1.3 | 3.1 | 0 | 1.1 |
| | $\overline{q}/q$, % | −0.1 | −0.1 | 0.7 | −37.2 | −32.4 | −0.5 | −1.2 | 3.2 | 0 | −1.1 |

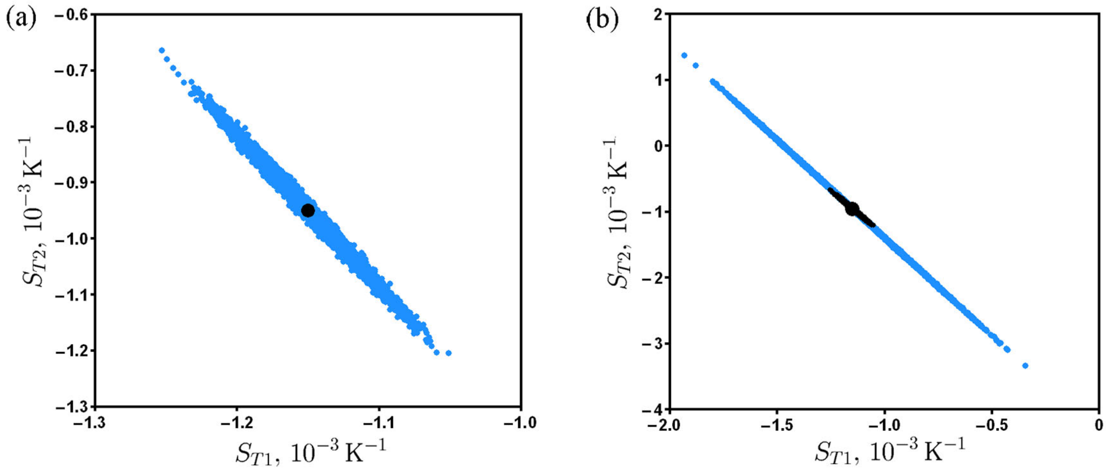

**Fig. 12.** Distribution of Soret coefficients $S_{T1}$ and $S_{T2}$ obtained from stationary refractive index differences and contrast factors with the added noise. Results for contrast factor Matrix 1 (a) and Matrix 2 (b). The black point corresponds to the mean values given in table 1. The data of plot (a) are shown in black color on plot (b).

the bias-corrected standard deviation $s$, the relative standard deviation $s/\overline{q}$ (%), and the relative error $\overline{q}/q$ (%) with respect to the exact value $q$ were calculated. One can see that the use of Matrix 2 with high condition number leads to a significant increase of relative errors and standard deviations in comparison with the results for Matrix 1, which has low condition number. The list of transport properties, from most to least sensitive to errors, is as follows: the cross-diffusion coefficients, main diffusion coefficients, thermal diffusion coefficients, eigenvalues, Soret coefficients. Increasing the number of points along the diffusion path can greatly improve the quality of results even in the case of ill-conditioned contrast factor matrix. In particular, for Matrix 2 with $R = 100$ the precision is very good for all transport properties except the cross-diffusion coefficients.

Let us now validate the determination of Soret coefficients from refractive index differences in the stationary state according to formula (37). To do this, we calculate $\Delta n_{s1}$, $\Delta n_{s2}$ from the values of Soret coefficients given in table 1 and add normally distributed random noise with the standard deviation $\sigma_{\Delta n} = 5 \times 10^{-6}$ and zero mean. To take into account possible errors in the determination of contrast factors, the normal noise with the standard deviation $\sigma_n = 10^{-4}$ is added to them as well (it corresponds to the relative standard deviation of 0.07–0.21%, which is realistic [16]). The results of simulation, where the Soret coefficients were determined from $10^4$ pairs of $\Delta n_{si}$ values, are shown in fig. 12. The use of Matrix 1 with low condition number leads to the following values of Soret coefficients and their standard deviations: $S_{T1} = (-1.15 \pm 0.03) \times 10^{-3}\,\mathrm{K}^{-1}$, $S_{T2} = (-0.95 \pm 0.07) \times 10^{-3}\,\mathrm{K}^{-1}$. In the case of Matrix 2 with high condition number, the results are $S_{T1} = (-1.15 \pm 0.20) \times 10^{-3}\,\mathrm{K}^{-1}$, $S_{T2} = (-0.96 \pm 0.58) \times 10^{-3}\,\mathrm{K}^{-1}$. Note that the variations of coefficients are not independent and populate some domain on the plane $(S_{T1}, S_{T2})$, see fig. 12. This domain appears when the linear transformation with the matrix $-\Delta T^{-1} N_C^{-1}$ is applied to the square ($\Delta n_{s1} \pm 3\,\sigma_{\Delta n}$, $\Delta n_{s2} \pm 3\,\sigma_{\Delta n}$), which contains more than 99% of all simulated points. The form of domain is also affected by the variations of contrast factors (in the considered case, their influence is rather small). For Matrix 2, the resulted domain has the form of a line due to the large condition number, which is related to the ratio of maximal and minimal eigenvalues according to (38). Comparison between steady and transient state methods for the determination of Soret coefficients shows that the latter method is much more robust since fitting of refractive index differences smoothes the experimental curves and eliminates most of random errors.

## 5 Results and discussion

In this section, we present the results of data processing and transport coefficient determination for DCMIX 1 experiment with the mixture THN (1), IBB (2), $n\mathrm{C}_{12}$ (3) with mass fractions 0.8/0.1/0.1 at 25 °C. Here the numbering of components is different from that used in sect. 4 and corresponds to the decrease of density. The mixture was contained in Cell 3 of the cell array with the height of $H = 5\,\mathrm{mm}$. We have processed Soret and Diffusion steps for 5 experimental runs with numbers 3, 8, 18, 23, 28. It was not possible to extract the values of transport coefficients from Run 13 due to poor quality of optical images. The contrast factor matrix for the two lasers with wavelengths 670 nm (1) and 935 nm (2) is presented in table 5 [17]. It has a rather large condition number $\mathcal{K} = 241$.

Let us first provide a detailed description of results for Run 3. The time sequence of this run was as follows. The mixture was first kept for 2 hours in isothermal conditions at the temperature of 25 °C (thermalization step). The interferometric images were recorded during the last 30 minutes of this step. Then the temperature difference $\Delta T = 10\,\mathrm{K}$ was applied. The readings of thermocouples at the top and bottom walls show how the temperature regime was established, see fig. 13(a). The Soret step

**Table 5.** Contrast factor matrix for the lasers with wavelengths 670 nm (1) and 935 nm (2) for ternary mixture THN (1), IBB (2), $n\mathrm{C}_{12}$ (3) with mass fractions 0.8/0.1/0.1 at 25 °C [17].

| $\partial n_1/\partial C_1$ | $\partial n_1/\partial C_2$ | $\partial n_2/\partial C_1$ | $\partial n_2/\partial C_2$ | Condition number $\mathcal{K}$ |
|---|---|---|---|---|
| 0.142741 | 0.088676 | 0.137344 | 0.083753 | 241 |

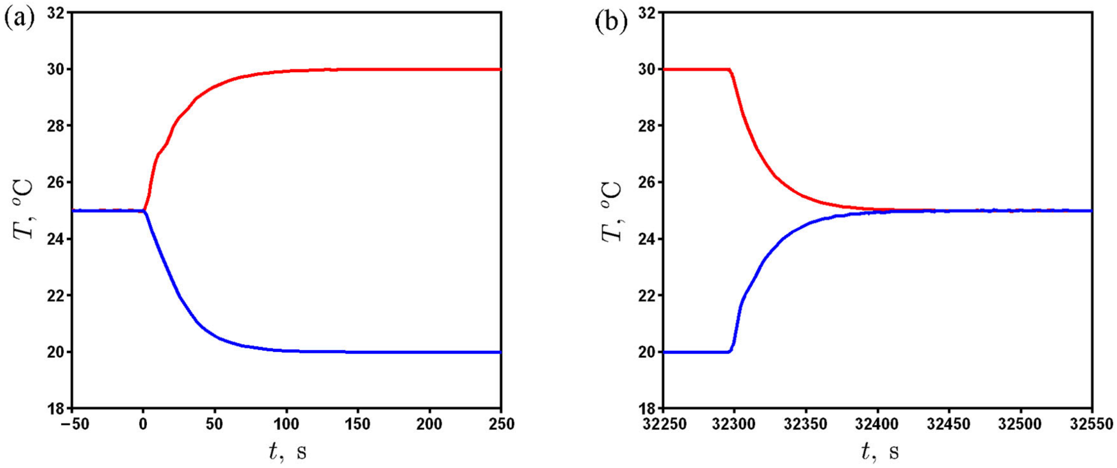

**Fig. 13.** The establishment of temperatures at the top and bottom walls in the beginning of Soret step (a) and diffusion step (b), Run 3.

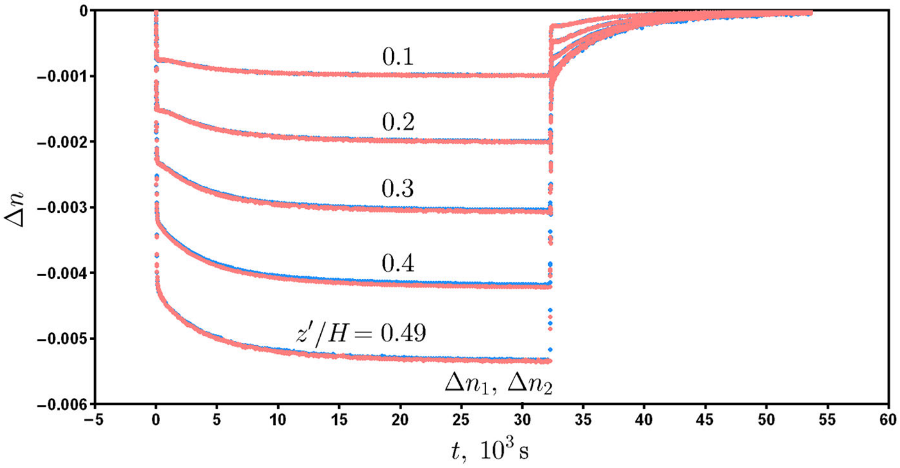

**Fig. 14.** The evolution of the differences of refractive indices $\Delta n_1$ (red) and $\Delta n_2$ (blue) with time at different positions during Soret and diffusion steps, Run 3.

lasted for 32295 seconds. Then the temperature difference was removed (fig. 13(b)), and the diffusion step continued for 21499 seconds. The evolution of refractive index differences $\Delta n_1$ and $\Delta n_2$ with time at different positions is shown in fig. 14. These curves were obtained by taking the reference image at the isothermal state ($t = 0$ in fig. 13(a)) and subtracting it from the subsequent images. Note that the original data for $\Delta n_1$ and $\Delta n_2$ contained different numbers of points in time. To provide a set of $M$ points taken at the same time moments as required by eq. (30), linear interpolation of data was used. The curves for $\Delta n_1$ and $\Delta n_2$ practically coincide due to the large condition number of the contrast factor matrix. Note that these curves describe the change of refractive indices induced by the changes of temperature and concentration of the mixture components.

To separate the concentration contribution for the Soret step, we took the reference image at time $t_0 = 193\,\mathrm{s}$ and subtracted it from all subsequent images. The optical data and thermocouple readings (fig. 13(a)) suggest that the linear temperature profile is already established by this moment of time. The chosen offset time corresponds to $7.6\,\tau_{\mathrm{th}}$, where $\tau_{\mathrm{th}} = H^2/\pi^2\chi$ is the relaxation time for temperature and $\chi$ is the thermal diffusivity (typical value for liquids $\chi = 10^{-7}\,\mathrm{m}^2/\mathrm{s}$ is assumed). The evolution of $\Delta n_1$ and $\Delta n_2$ during the Soret step is shown in fig. 15(a). One can see that the steady-state separation is not completely achieved. The resulting curves for the diffusion step

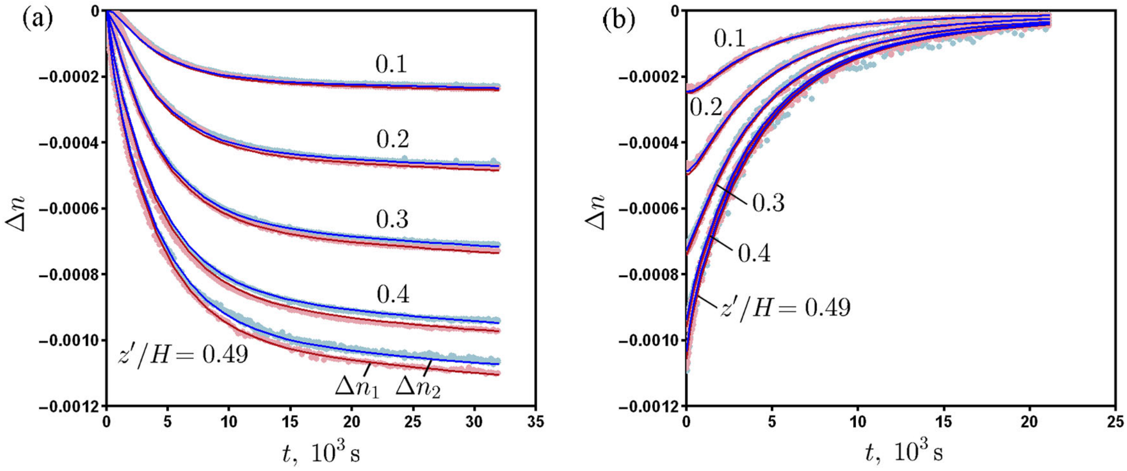

**Fig. 15.** The evolution of the differences of refractive indices $\Delta n_1$ (red) and $\Delta n_2$ (blue) with time at different positions during the Soret step (a) and diffusion step (b), Run 3. The zero-time moment corresponds to 193 s for the Soret step and to 32487 s for the diffusion step, see figs. 13 and 14. Solid lines correspond to the fitted analytical solution.

**Table 6.** Results of calculations for Run 3 with different numbers of points $R$.

| Points | Soret step | | | | Diffusion step | | | |
|---|---|---|---|---|---|---|---|---|
| $R$ | $\lambda_1$ | $\lambda_2$ | $S_{T1}$ | $S_{T2}$ | $\lambda_1$ | $\lambda_2$ | $S_{T1}$ | $S_{T2}$ |
| | $10^{-10}$ m$^2$/s | | $10^{-3}$ 1/K | | $10^{-10}$ m$^2$/s | | $10^{-3}$ 1/K | |
| 1 | 3.09 | 8.97 | 1.27 | −0.57 | 2.87 | 8.43 | 2.20 | −2.12 |
| 2 | 0.37 | 6.43 | 1.19 | −0.21 | 2.39 | 7.31 | 2.08 | −1.95 |
| 4 | 0.38 | 6.38 | 1.06 | −0.31 | 2.26 | 7.15 | 1.87 | −1.61 |
| 8 | 0.37 | 6.34 | 1.22 | −0.28 | 2.16 | 7.06 | 1.79 | −1.48 |
| 16 | 0.36 | 6.32 | 1.44 | −0.64 | 2.05 | 6.95 | 1.71 | −1.36 |
| 23 | 0.36 | 6.30 | 1.20 | −0.24 | 2.06 | 6.95 | 1.69 | −1.33 |
| 46 | 0.36 | 6.29 | 1.18 | −0.22 | 2.02 | 6.91 | 1.67 | −1.30 |
| 92 | 0.36 | 6.29 | 1.29 | −0.39 | 2.00 | 6.89 | 1.66 | −1.27 |
| 184 | 0.36 | 6.29 | 1.33 | −0.47 | 1.99 | 6.89 | 1.65 | −1.26 |
| 368 | 0.36 | 6.29 | 1.34 | −0.48 | 1.99 | 6.89 | 1.65 | −1.26 |

are shown in fig. 15(b). In this case, the reference image corresponds to the isothermal state ($t = 0$). The time offset $t_0 = 192$ s from the end of Soret step ($t = 32295$ s) was taken to ensure that the temperature gradient is removed, see fig. 13(b).

The results of calculations for Run 3 are shown in table 6. The eigenvalues and Soret coefficients were determined from the data of Soret and diffusion steps for different numbers of points $R$ along the diffusion path. The total number of points in the $z$-direction in the images is 736, so the possible values of $R$ correspond to the divisors of $736/2 = 368$. With increasing $R$, convergence of results is observed. There is a good agreement between values of $\lambda_2$ and $S_{T1}$ for Soret and Diffusion steps for large $R$, while the values of $S_{T2}$ and especially $\lambda_1$ disagree.

To understand the reasons of such disagreement, let us analyze the behaviour of the error function $E$ given by (31), (33). It is convenient to treat it as a function of relaxation times $\tau_j = H^2/\pi^2\lambda_j$, $j = 1, 2$. First of all, this function satisfies $E(\tau_1, \tau_2) = E(\tau_2, \tau_1)$. When $\tau_1$ and $\tau_2$ are exchanged, the columns of matrix $K$ in eq. (26) are exchanged as well, so the final expressions for $\Delta n_1$ and $\Delta n_2$ remain unaltered. The plots of error function $E(\tau_1, \tau_2)$ for the Soret and diffusion steps in Run 3 are shown in fig. 16. One can see that this function has a ravine-type shape. The point corresponding to the minimum of $E$ is well defined in $\tau_2$ direction. At the same time, large variations of $\tau_1$ produce small variations of the error function $E$. Thus, $\tau_1$ cannot be determined accurately. Due to the large scattering of results for $\lambda_1$, we do not provide the values of diffusion and thermal diffusion coefficients, which essentially depend on both eigenvalues. The apparent reasons for that are incomplete separation (homogenization) in the Soret (Diffusion) step and reduced separation due to non-linearity of temperature field in the $y$-direction (which is expected to be the same as in the $x$-direction, see figs. 7 and 10). Note that the observed separation results from the concentration field averaged in the $y$-direction (along

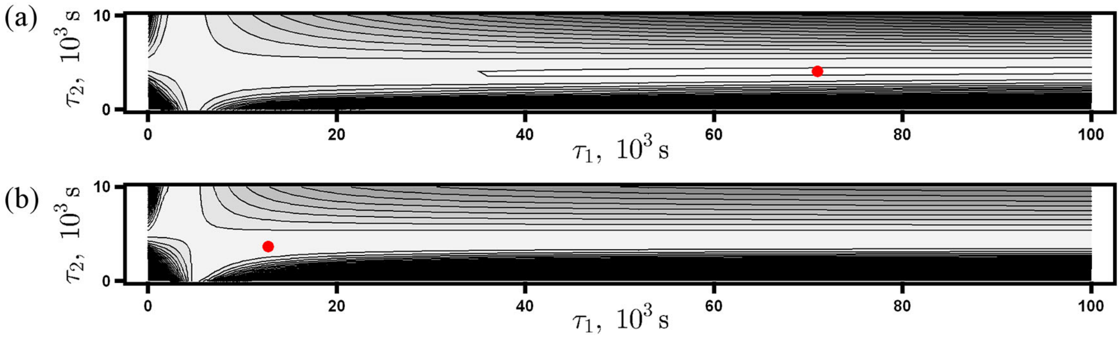

**Fig. 16.** The isolines of error function $E(\tau_1, \tau_2)$ for the Soret step (a) and diffusion step (b) of Run 3, $R = 368$. The red dots correspond to minimum of $E$, which is reached at $\tau_1 = 70973$, $\tau_2 = 4030$ for the Soret step and at $\tau_1 = 12740$, $\tau_2 = 3679$ for the diffusion step. The corresponding eigenvalues are given in table 6.

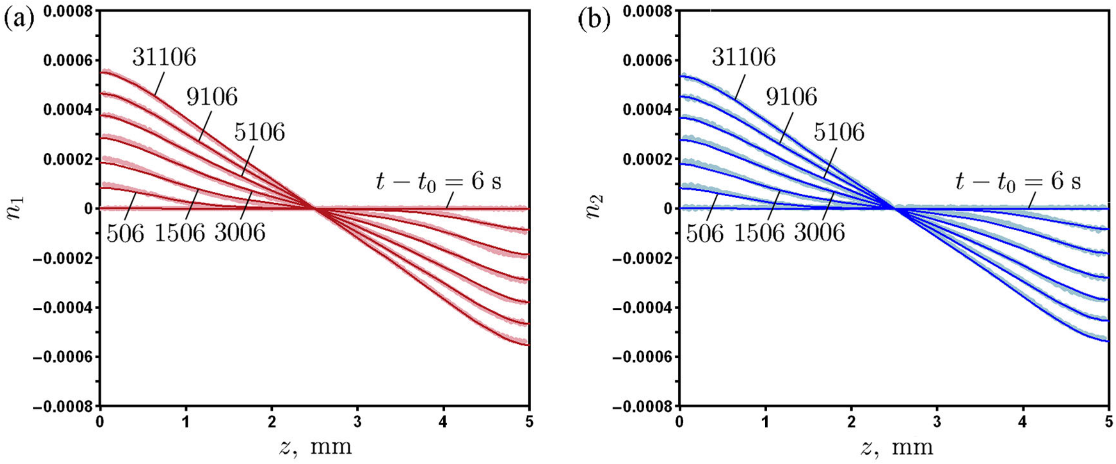

**Fig. 17.** The evolution of refractive index profiles for $n_1$ (a) and $n_2$ (b) with time during the Soret step of Run 3. Solid lines correspond to the fitted analytical solution.

the optical path). The above uncertainties coupled with ill-conditioned contrast factor matrix made it impossible to determine $\tau_1$ accurately. Note that the latter reason itself could not affect the results so drastically since the test calculations with ill-conditioned matrix in sect. 4 allowed us to determine the transport coefficients accurately.

The evolution of refractive index profiles with time during the Soret step is presented in fig. 17. The experimental data are shown along with the fitted theoretical curves for $R = 368$. The fitting is performed with the help of eq. (34) with $t_0 = 193\,\mathrm{s}$. The obtained eigenvalues are given in table 6, while the elements of $K$ matrix are as follows: $K_{11} = -3.814335\times10^{-4}$, $K_{12} = -11.114110\times10^{-4}$, $K_{21} = -3.572971\times10^{-4}$, $K_{22} = -10.866410\times10^{-4}$. Equation (34) can be written in the form

$$\Delta\boldsymbol{n}_{\mathrm{theor}}(t_0 + t, z') = \Delta\boldsymbol{n}_{\mathrm{exper}}(t, z') + \Delta\boldsymbol{n}_{\mathrm{theor}}(t_0, z'), \tag{39}$$

where $\Delta\boldsymbol{n}_{\mathrm{exper}}(t, z')$ is the experimentally measured difference of refractive indices, and $\Delta\boldsymbol{n}_{\mathrm{theor}}(t, z') = K\Delta\boldsymbol{w}(t, z')$ is the theoretical prediction based on analytical solution. Equation (39) shows how the experimental data must be corrected to account for separation during the establishment of temperature gradient. The corrected refractive index profiles are presented in fig. 18. They are reconstructed from (39) assuming that the deviations of refractive indices from those corresponding to the reference image are zero at the mid-height of the cell and profiles are antisymmetric with respect to the point $z = H/2$, $n_i = 0$. The solid lines (points) correspond to the values on the left-hand (right-hand) side of (39). The profiles shown in fig. 17 correspond to the first term on the right-hand side of (39). One can see that the corrected profiles provide accurate description of separation near the top and bottom walls of the cell. The curves for $t = \infty$ correspond to the anticipated separation at the steady state according to (36).

The summary of obtained results for all runs is presented in table 7. The Soret coefficient of $n\mathrm{C}_{12}$ is calculated as $S_{T3} = -S_{T1} - S_{T2}$. The eigenvalue $\lambda_2$ and the Soret coefficients $S_{T1}$, $S_{T2}$ determined in different runs within each step show acceptable agreement. However, the Soret coefficient $S_{T2}$ obtained from the diffusion step is almost two times larger in magnitude than that obtained from the Soret step. Unfortunately, the eigenvalue $\lambda_1$ cannot be accurately determined due to large scattering of

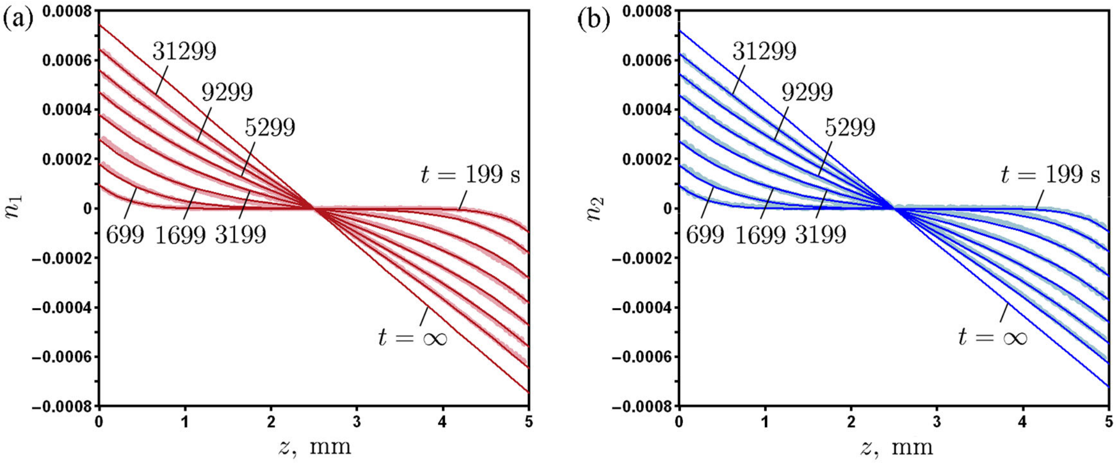

**Fig. 18.** The evolution of corrected refractive index profiles for $n_1$ (a) and $n_2$ (b) with time during the Soret step of Run 3. The profiles are corrected to account for the separation during the establishment of temperature regime. Solid lines correspond to the fitted analytical solution. The curves for $t = \infty$ correspond to the anticipated separation at the steady state.

**Table 7.** Summary of results for Soret and diffusion steps. Number of points in space $R = 368$.

| Step | Run | $\lambda_1$ | $\lambda_2$ | $S_{T1}$ (THN) | $S_{T2}$ (IBB) | $S_{T3}$ ($n\mathrm{C}_{12}$) |
|---|---|---|---|---|---|---|
| | | $10^{-10}$ m$^2$/s | | $10^{-3}$ 1/K | | |
| Soret | 3 | 0.36 | 6.29 | 1.34 | −0.48 | −0.86 |
| | 8 | 0.60 | 6.78 | 1.21 | −0.27 | −0.94 |
| | 18 | 0.60 | 6.82 | 1.65 | −0.97 | −0.68 |
| | 23 | 0.55 | 6.56 | 1.43 | −0.64 | −0.79 |
| | 28 | 0.54 | 6.77 | 1.38 | −0.51 | −0.87 |
| | Mean value | $0.53 \pm 0.10$ | $6.64 \pm 0.22$ | $1.40 \pm 0.16$ | $-0.57 \pm 0.26$ | $-0.83 \pm 0.10$ |
| Diffusion | 3 | 1.99 | 6.89 | 1.65 | −1.26 | −0.39 |
| | 8 | 0.07 | 6.13 | 1.24 | −0.64 | −0.60 |
| | 18 | 0.19 | 6.22 | 1.56 | −1.15 | −0.41 |
| | 23 | 0.08 | 6.16 | 1.52 | −1.08 | −0.44 |
| | 28 | 0.25 | 6.21 | 1.47 | −1.00 | −0.47 |
| | Mean value | $0.52 \pm 0.83$ | $6.32 \pm 0.32$ | $1.49 \pm 0.15$ | $-1.03 \pm 0.24$ | $-0.46 \pm 0.08$ |

results. The eigenvalue $\lambda_2$ and the Soret coefficient $S_{T1}$ demonstrate good agreement for all runs in both Soret and diffusion steps. The values of Soret coefficients provided for the Benchmark correspond to the Soret step. We think that these results are more reliable since the experimental time of Soret step was 1.5 times larger than that of diffusion step in all runs. However, fig. 15(a) and fig. 18 show that the complete separation was not achieved even in the Soret step of extended Run 3. Note that the experimental time in the rest of the runs was smaller than in Run 3 (around 21500 seconds for the Soret step and 14000 seconds for the diffusion step).

Let us now discuss the experimental error in the Soret coefficients (see table 7). The largest standard deviation is obtained for $S_{T2}$ (IBB), the medium one corresponds to $S_{T1}$ (THN), while the smallest one is found for $S_{T3}$ ($n\mathrm{C}_{12}$). Due to a small number of available experimental runs, one may ask whether the obtained standard deviations give a reliable estimation of experimental error. Note that real experimental measurements contain not only random, but also systematic errors, which cannot be eliminated by fitting analytical solution to the experimental data (as it was done in sect. 4).

The impact of errors on the stationary values of $\Delta \boldsymbol{n}_s$, which are related to the fitted matrix $K$ by formula (36), can be estimated by performing simulations on the basis of eq. (37) with the prescribed level of noise in $\Delta \boldsymbol{n}_s$. To estimate the level of noise, we analyzed the refractive index differences $\Delta n_1(t, z')$ and $\Delta n_2(t, z')$, $0 < z' < H/2$ during 30 minutes before the start of experiment (thermalization step). In the absence of temperature and concentration gradients, these differences should be ideally zero.

**Table 8.** Mean values and standard deviations of refractive index differences $\Delta n_1(t, z')$ and $\Delta n_2(t, z')$ during thermalization step at 25 °C.

| Run | $\Delta n_1 \times 10^6$ | $\Delta n_2 \times 10^6$ |
|---|---|---|
| 3 | $0.30 \pm 2.80$ | $0.34 \pm 2.35$ |
| 8 | $-0.01 \pm 3.01$ | $0.68 \pm 3.88$ |
| 18 | $0.09 \pm 2.65$ | $1.16 \pm 3.10$ |
| 23 | $1.36 \pm 3.29$ | $0.21 \pm 4.19$ |
| 28 | $-0.61 \pm 3.07$ | $0.90 \pm 3.17$ |
| Average | $0.23 \pm 2.96$ | $0.66 \pm 3.34$ |

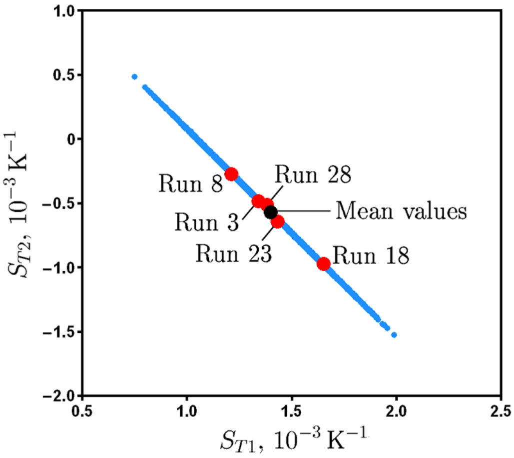

**Fig. 19.** The values of Soret coefficients $S_{T1}$ and $S_{T2}$ measured in Soret step of different runs and distribution of these coefficients obtained from stationary refractive index differences with the added noise.

The recorded fluctuations show the typical level of noise, whose statistical characteristics are presented in table 8. Based on these data, we performed simulation on determining the Soret coefficients from eq. (37). The normally distributed noise with the standard deviation $3 \times 10^{-6}$ and zero mean was added to the values of $\Delta n_{1s}$ and $\Delta n_{2s}$, which correspond to the mean values of $S_{T1}$ and $S_{T2}$ for the Soret step in table 7 ($10^4$ points were taken). The obtained distribution of Soret coefficients and the results from real experimental runs are shown in fig. 19. The simulation provided the following results: $S_{T1} = (1.38 \pm 0.17) \times 10^{-3}\,\mathrm{K}^{-1}$, $S_{T2} = (-0.54 \pm 0.28) \times 10^{-3}\,\mathrm{K}^{-1}$. The obtained standard deviations are very close to those given in table 7. If the noise in contrast factor matrix $N_C$ with standard deviation $10^{-4}$ is taken into account, the deviations become somewhat larger: $S_{T1} = (1.38 \pm 0.19) \times 10^{-3}\,\mathrm{K}^{-1}$, $S_{T2} = (-0.55 \pm 0.32) \times 10^{-3}\,\mathrm{K}^{-1}$. Note that the simulated and measured variations of Soret coefficients are not independent. They show a linear correlation due the large condition number of contrast factor matrix (see fig. 19 and discussion in sect. 4).

## 6 Conclusion

In this paper, we have processed the data of space experiment DCMIX 1, which is devoted to the measurement of diffusion and Soret coefficients for ternary mixture of 1,2,3,4-tetrahydronaphthalene, isobutylbenzene and *n*-dodecane at mass fractions of 0.8/0.1/0.1 and at 25 °C. The measurements were performed on the ISS with the help of optical digital interferometry. The raw interferometric images were processed to obtain the temporal and spatial evolution of refractive indices for two laser beams of different wavelengths. The method for extracting the diffusion and thermal diffusion coefficients originally developed for Optical beam deflection was extended to optical digital interferometry allowing for the spatial variation of refractive index along the diffusion path. The method was validated and applied to processing the data for Soret and diffusion steps in 5 experimental runs. The obtained results for the Soret coefficients and one of the eigenvalues of diffusion matrix showed acceptable agreement within each step. The second eigenvalue was not determined with sufficient accuracy.

This work was performed in the frame of DCMIX project (ESA-Roscosmos) and supported by FGUP TSNIIMASH. The authors are grateful to A. Mialdun, V. Shevtsova, and W. Köhler for useful discussions.

## References

1. K. Ghorayeb, A. Firoozabadi, T. Anraku, SPE J. **8**, 114 (2003).
2. S. Wiegand, J. Phys.: Condens. Matter. **16**, 357 (2004).
3. A. Mialdun, V.M. Shevtsova, J. Chem. Phys. **134**, 044524 (2011).
4. V.M. Buzmakov, A.Yu. Pinyagin, A.F. Pshenichnikov, J. Eng. Phys. Thermophys. **44**, 529 (1983).
5. I. Ryzhkov, Fluid Dyn. **48**, 477 (2013).
6. R. Monti (Editor), *Physics of Fluids in Microgravity* (Taylor & Francis, London, 2001).
7. Q. Kemao, Opt. Lasers Eng. **45**, 304 (2007).
8. L. Huang *et al.*, Opt. Lasers Eng. **48**, 141 (2010).
9. D. Ghiglia, M. Pritt, *Two-Dimensional Phase Unwrapping: Theory, Algorithm, and Software* (Wiley, 1998).
10. A. Pati, P. Rastogi, Opt. Lasers Eng. **43**, 475 (2005).
11. K.B Haugen, A. Firoozabadi, J. Phys. Chem. B. **110**, 17678 (2006).
12. A.D. Polyanin, *Handbook of Linear Partial Differential Equations for Engineers and Scientists* (CRC Press, 2001).
13. A. Mialdun, V.M. Shevtsova, Int. J. Heat Mass Transf. **51**, 3164 (2008).
14. A.J. Nelder, R. Mead, Comput. J. **7**, 308 (1965).
15. V. Shevtsova, V. Sechenyh, A. Nepomnyashchy, J.C. Legros, Philos. Mag. **91**, 3498 (2011).
16. A. Königer, H. Wunderlich, W. Köhler, J. Chem. Phys. **132**, 174506 (2010).
17. V.V. Sechenyh, J.C. Legros, V. Shevtsova, J. Chem. Thermodyn. **62**, 64 (2013).